American Society of Mechanical Engineers

ASME Accepted Manuscript Repository

Institutional Repository Cover Sheet

Cranfield Collection of E-Research - CERES

ASME Paper Title: Integrated power and thermal management system for a hybrid-electric aircraft: integrated modelling and passive cooling analysis

Authors: Zeyu Ouyang, Theoklis Nikolaidis, Soheil Jafari

ASME Journal Title: Journal of Engineering for Gas Turbines and Power

Volume/Issue: Date of Publication (VOR* Online): 22 July 2024

ASME Digital Collection URL: https://asmedigitalcollection.asme.org/gasturbinespower/article/doi/10.1115/1.4066050/1201729/Integrated-Power-and-Thermal-Management-System-for

DOI: https://doi.org/10.1115/1.4066050

*VOR (version of record)

Proceedings of ASME Turbo Expo 2024
Turbomachinery Technical Conference and Exposition
GT2024
June 24-28, 2024, London, United Kingdom

GT2024-121232

INTEGRATED POWER AND THERMAL MANAGEMENT SYSTEM FOR A HYBRID-ELECTRIC AIRCRAFT: INTEGRATED MODELLING AND PASSIVE COOLING ANALYSIS

Zeyu Ouyang[1] **Theoklis Nikolaidis[1]** **Soheil Jafari[2]**

[1]Centre for Propulsion and Thermal Power Engineering, School of Aerospace Transport and Manufacturing (SATM)
Cranfield University, Cranfield MK43 0AL, UK
[2]Former, Centre for Propulsion and Thermal Power Engineering
School of Aerospace Transport and Manufacturing (SATM)
Cranfield University, Cranfield MK43 0AL, UK

ABSTRACT

Aircraft electrification introduces challenges in power and thermal management. In a hybrid-electric aircraft (HEA), the additional heat loads generated by the high-power electrical components in the propulsion system can negate the benefits of the HEA. Consequently, an integrated energy management system is required for the HEA to reject the additional heat loads while minimizing energy consumption.

This paper presents the integrated modelling method for an integrated power and thermal management system (IPTMS) for HEA. With this method, a platform can be developed to assess the varying efficiencies of the components in the electrical propulsion system (EPS), such as the battery, motor, bus, and converter, and the performance of the thermal management system (TMS), such as passive cooling, during a flight mission. This makes it applicable to modular designs and optimizations of the IPTMS. A small/medium range (SMR) aircraft similar to ATR72 is studied to demonstrate the platform's capabilities. In this study, the EPS operates only during take-off and climb. It provides supplementary propulsive power, which declines linearly from 924 kW to zero. Therefore, the platform assesses the heat and power loads of the IPTMS for a typical flight mission (take-off and climb) in this study. The performance of passive cooling is also analysed across this typical flight mission and under normal, hot-day, and cold-day conditions. It was found that under the normal condition, after the mid-climb flight mission, the EPS components except for the motor and the inverter can be cooled sufficiently by the passive cooling mechanism without any need for active cooling. However, the battery temperature decreases below its minimum operating temperature (15 oC) after the late-climb segment indicating the need for active temperature control to prevent damage. The passive cooling is still sufficient under the hot-day and cold-day conditions. Additionally, compared with the normal condition, the points at which passive cooling is sufficient to cool the component move forward in the hot-day condition and backward in the cold-day condition, respectively. Under the hot-day condition, the battery temperature is below its minimum temperature after the late-climb, still requiring active temperature control. In the cold-day condition, the bus, the converter, and the battery require active temperature control to prevent their temperatures below the minimum temperatures. Additionally, the heat from the gas turbine engine has a positive impact to ensure the motor and the inverter operate at their operating temperatures in cold conditions. The studied aircraft can be assessed with the integrated model under normal, hot-day, and cold-day conditions for heat and power loads, as well as passive TMS performance. This demonstrates the adaptability of the integrated modelling method. These findings imply the potential to minimize TMS weight and energy consumption, providing an insight for further research on IPTMS.

Keywords: Thermal management, power management, integrated power and thermal management, hybrid-electric aircraft, passive cooling mechanism

NOMENCLATURE

AC	alternating current
BC	battery-converter
BL	baseline
CP	cooling power
D	diameter
DC	direct current
DP	design point
dP	pressure drop
EPS	electrical propulsion system
HEA	hybrid-electric aircraft
HX	heat exchanger
I	current

Published by ASME. This is the Author Accepted Manuscript issued with: Creative Commons Attribution License (CC:BY 4.0).
The final published version (version of record) is available online at DOI:10.1115/1.4066050. Please refer to any applicable publisher terms of use.

I_{ref}	reference maximum current
K_I	exponent of current
K_V	exponent of voltage
MI	motor-inverter
MTOW	maximum take-off weight
N_{fin}	number of fins
P	power
PDS	power distribution system
PS	power switch
REC	rectifier
SOC	state of charge
T	temperature
TMS	thermal management system
T/O	take-off
SMR	small/medium range
V_{ref}	reference maximum voltage
W	mass flow rate

SUBSCRIPTS

bat	battery
con	converter
cond	conduction
em	electrical machine
in	input
inv	inverter
max	maximum
min	minimum
mot	motor
out	output
sw	switching

1 INTRODUCTION

Nowadays, global and regional organisations have proposed ambitious emission reduction goals, such as the Flight Path 2050 plans to reduce 75% CO2 and 90% NOx [1], and NASA [2] aims to reduce 80% NOx for the next generation of aircraft. Hybrid-electric aircraft (HEA) have been widely studied to meet the requirements of greener aviation. However, their additional high-power components generate heat loads, offsetting the benefits offered by HEA [3].

The UK's Aerospace Technology Institute (ATI) has focused on innovative thermal management systems for electrified propulsion aircraft (EPA) [4]. Other institutions [5–7] also have researched the novel aircraft energy management, named Integrated Power and Thermal Management System (IPTMS). Their IPTMS research focuses on the architecture design [5,8], the power management design [7], the system modelling [6], and the development of optimisation and analysis methods [9,10].

Some existing studies on TMS or IPTMS for HEA assess the heat loads using fixed-efficiency methods and neglect the effect of passive cooling [8,11,12]. When using a fixed-efficiency method to assess, the heat loads of the electrical propulsion system (EPS) decrease when the propulsive power of a HEA is reduced. However, the heat loads of some components (e.g., motor) do not decrease in some situations, such as at a constant rotational speed condition. The authors in [13] developed a platform for HEA to assess the varying efficiencies of the components of EPS under different power requirements, but some components, such as the inverter and the converter, were still modelled by using the fixed-efficiency method. For a regional HEA that can reach a flight altitude of higher than 5 km, the ambient temperature can drop below -18 ℃. Therefore, the advantage of low ambient temperature at high altitudes should be utilized to optimise the energy consumption for cooling. Under these low-power and high-altitude conditions, if the passive cooling mechanism is sufficient, there is little, or no energy required for the TMS. The literature focusing on the passive cooling mechanism is relatively limited. In [14], the study designed a passive cooling method, called passive Outer Mold Line (OML) cooling. This cooling method uses the exiting OML of the aircraft as a heat sink. The heat from the components is transferred to the OML and is rejected to the aircraft skin, and the skin is then cooled by the ambient air. This type of passive cooling does not require the use of ram air and any additional power for cooling, but it incurs a weight penalty of TMS. Additionally, the authors in [15] investigated the OML cooling for a mega-watt aircraft, and it was found that the required area of the minimum-efficiency OML cooling exceeds the available area, implying that the OML cooling should be used with other cooling strategies. Moreover, Coutinho et al. [16] investigated the passive cooling mechanism with aircraft skin heat exchangers. They found that compared with the conventional phase-change cooling, the passive cooling can sufficiently cool the components without ram air drag, but the weight and size of the skin heat exchanger introduces challenges in installation.

Other studies have also conducted research on how to minimize the weight penalty due to hybridisation. Lents et al. extended their previous work and implemented a passive cooling mechanism, called battery heat acquisition [17,18]. With this technique, the battery can be pre-cooled on the ground to reduce the TMS weight and required power by reducing the thermal requirements. They found that the weight of heat exchangers can be reduced 80%, but the fuel consumption was increased 0.75% due to the drag, power, and weight of the TMS. They also proposed a weight sensitive study [3] and found that 1% improvement in the battery efficiency and 2% in the motor efficiency can decrease the weight of their heat exchangers by 26% and 38%, respectively. Kim et al. proposed a trade-off study for the IPTMS of a megawatt HEA at the system level [19]. In that study, three cooling strategies were assessed: 1) liquid (fuel) cooling, 2) vapor cycle system, and 3) hybrid cooling. They found that the IPTMS was not feasible at their technological level. Additionally, they found that the advancement in TMS is more urgent than in power distribution technologies to overcome the weight penalty due to the hybridisation. The implementation of air cooling has been studied for HEA to reduce TMS weight. Abolmoali et al. [20] designed an IPTMS for a long-endurance unmanned series HEA by integrating the propulsion system and the TMS. They implemented fuel as the coolant to reduce TMS weight and increase the GT engine thermal efficiency. It was found that compared with the baseline aircraft, the series HEA

consumes 750 lb less fuel but gains 708 lb in weight. NASA ULI [21–23] designed a TMS for a turboelectric aircraft. In their design, the battery can be sufficiently cooled by the air from the environmental control system (ECS). For other components, they proposed and compared the performance of three cooling strategies: 1) oil, 2) additional PAO (polyalphaolefin) coolant, and 3) phase-change material (PCM) cooling. It was found that the oil cooling was not sufficient at take-off and climb mission phases. During these phases, the additional PAO and the PCM cooling were suggested to be implemented. Compared with the PCM cooling, the additional PAO cooling is much heavier, causing more fuel burn. Kellermann et al. [24] designed ram air-based cooling TMS for a short-range HEA and conducted sensitive analysis for fuel burn. It was found that if the electric component junction temperature can be increased to 400K, the drag due to the ram air-based TMS can be eliminated. However, the fuel burn will be increased by 0.19% under a more realistic temperature condition of 380 K. Adler et al. [25] optimised the phase-change cooling, replacing the vapor cycle chiller by a thermoacoustic chiller, which consumes acoustic power, such as the waste heat, from the engine rather than electrical power from the battery. The thermoacoustic chiller uses the reversed cycle of the thermoacoustic engine to cool the battery coolant. Compared with the conventional phase-change cooling, this cooling method causes 1.62% more fuel burn due to pressure losses during the heat extraction from the engine, but it could be more beneficial at low-altitude conditions.

Compared with other active cooling strategies, air cooling has more significant advantage in minimizing TMS weight because it has less requirements, such as it does not need pumps, air-liquid heat exchangers, and shorter distribution systems due to its open-loop cooling mechanism. However, the air-based TMS causes additional drag, increasing fuel consumption. Additionally, its feasibility is restricted under high-power conditions. Therefore, an integrated modelling method for EPS and TMS can help with the trade-off study for different cooling strategies, by analysing the increased weight, induced drag, and power usage of the TMS. The integrated modelling method should also involve passive cooling mechanism. In low-power and high-altitude conditions, a passive cooling mechanism, involving air natural convection and radiation, is potentially sufficient. This passive cooling eliminates the need for active cooling and does not add additional weight to the TMS. In a HEA, the power loads of the EPS affect both the sizes of the components and their heat loads, while the surfaces of the components impact the passive cooling performance. It is necessary to analyse the capability of passive cooling in multiple energy (thermal and power) domains.

This paper presents an integrated modelling method for IPTMS's analytical models by combining EPS and TMS modelling methods. The methodology is adaptable to be used in a variety of IPTMS designs as well. With this modelling method, this paper investigates the performance of passive cooling under normal, hot-day, and cold-day conditions, which demonstrates the adaptability. In this paper, a small/medium range (SMR) aircraft similar to ATR72 is studied. It was found that, in the normal condition, after the start of the climb and the mid-climb, the bus and the converter-battery loop can be sufficiently cooled by passive cooling. In the case of hot day or cold day, the point, where the passive cooling is sufficient to cool the component, move forward or backward, compared with the normal condition. Because the passive cooling is sufficient, active cooling is not needed for the components after those flight segments, reducing thermal requirements and potentially minimizing the weight and volume of the TMS. However, in the cold-day condition, the temperatures of the bus, the converter, and the battery are below their minimum temperature after the late-climb, which introduces challenges to the TMS active cooling design. The methodology of this study for integrated modelling and passive cooling analysis is shown in Figure 1. First, a HEA architecture was designed for the baseline (BL) aircraft, and an IPTMS architecture was then developed for the HEA. After that, an IPTMS platform was developed by integrating the EPS and the TMS. With the platform, the HEA weight, the heat and power loads were assessed. Additionally, the passive cooling performance under the normal, hot-day, and cold-day conditions was assessed. Finally, the requirements and challenges of the IPTMS design and the capability of the passive cooling were investigated by analysing the results. This paper is organized as follows. Section 2 presents the methodology of the integrated modelling to develop an IPTMS platform, which includes the architecture of the IPTMS, the integration of the EPS, and the TMS design. Section 3 introduces the studied case. Section 4 shows and discusses the results of the IPTMS platform, including the comparison of weight, the assessment of heat and power loads, and the evaluation of passive cooling performance. Finally, a conclusion is presented in Section 5.

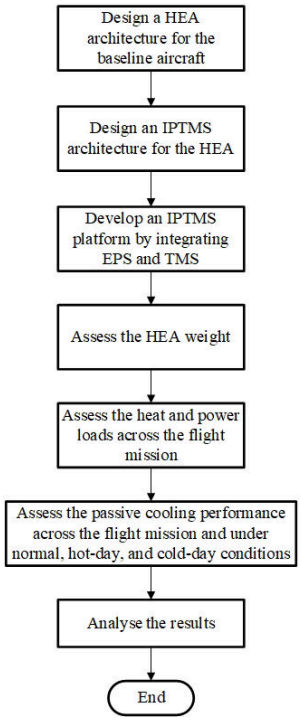


Figure 1 Methodology flowchart

2 METHODOLOGY OF INTEGRATED MODELLING

Several studies have investigated the impacts of series and parallel configurations of HEA [11,26]. They found that the series HEA generally has more weight and heat than the parallel HEA. A parallel HEA configuration was decided for the BL aircraft as an initial study.

Figure 2 shows the IPTMS architecture for the parallel HEA. The IPTMS comprises two propulsion systems: 1) the EPS and 2) the gas turbine (GT) system. In Figure 2, the blue and black blocks represent electrical and mechanical components, respectively. The heat and power loads of the IPTMS are shown in Table 1. In this study, only the performance of EPS and TMS are assessed.

In the EPS, the battery, as the power source in the EPS, supplies voltage and current to the system. Under a constant power output condition, the battery voltage decreases as its state of charge (SOC) decreases, which leads to variations in the battery voltage during the flight mission. As a result, the converter is needed to convert the varying input voltage to a nearly constant output voltage for the power distribution system (PDS). With a constant voltage, power can be distributed steadily to different power users. Because the battery provides high DC power, the PDS is designed to be a DC distribution to minimize the loss due to the DC-to-AC transmission. In the PDS, the DC bus distributes the power to terminal power users, such as coolant pumps, (ram) air fans, and motors. The motors in this design are AC motors, requiring AC input voltage, so they need inverters to convert the DC power/voltage in PDS to the required AC power/voltage.

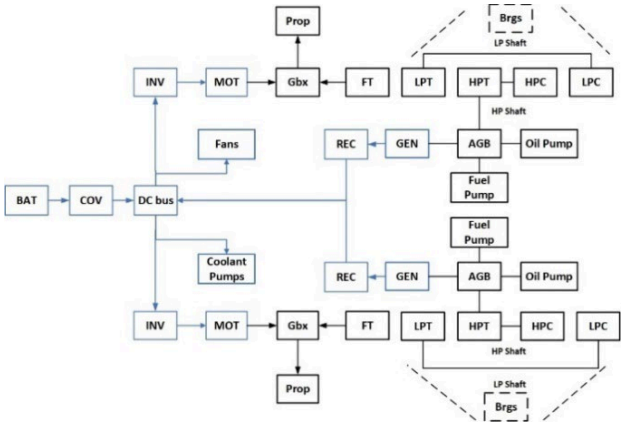


Figure 2 IPTMS architecture for parallel HEA (MOT: motor, INV: inverter, CON: converter, BAT: battery, GEN: generator, REC: rectifier, Prop: propeller, Gbx: power gearbox, FT: free turbine, LPT: low-pressure turbine, HPT: high-pressure turbine, HPC: high-pressure compressor, LPC: low-pressure compressor, Brgs: shaft bearings, and AGB: auxiliary gearbox)

In the GT system, the high-pressure turbines (HPTs) drive the generators as well as the fuel and oil pumps via the accessory gearboxes (AGBs). The engine-driven generators provide power for the power users in the cabin, and the power can also be used for cooling EPS. In the IPTMS, the power from generators is transferred from AC to DC power by the rectifiers and is distributed to the pumps and fans. The FTs are coupled with the motors through the power gearboxes to drive the propellers.

Table 1 Considered heat and power loads of the subsystems of IPTMS

Subsystem/Component	Considered Load
EPS	
motor	heat, power
inverter	heat, power
bus	heat, power
converter	heat, power
battery	heat, power
GT	
power gearbox	heat, power
shaft bearings	heat
auxiliary gearbox	heat, power
TMS	
pumps	heat, power
fan	heat, power

The development of the IPTMS platform comprises two sections: 1) the integration of the EPS models and 2) the TMS design. In this study, the platform was developed to evaluate the heat and power loads of the IPTMS and the passive cooling performance. Through the integration of the EPS models, the components were modelled and sized to satisfy the required propulsive power and system voltage of the EPS. Their volumes and geometries then affected the passive cooling performance. After the integration of the EPS, the platform assessed the heat and power loads of the EPS and the capability of the passive cooling.

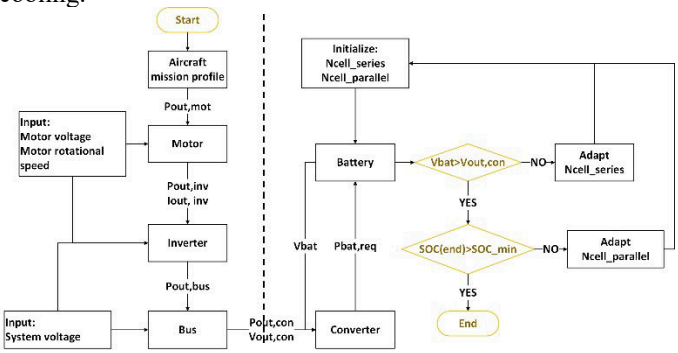


Figure 3 Flowchart of model integration for EPS ($P_{out,mot}$: motor output power, $P_{out,inv}$: inverter output power, $I_{out,inv}$: inverter output current, $P_{out,bus}$: bus output power, $P_{out,con}$: converter output power, $V_{out,con}$: converter output voltage, V_{bat}: battery output voltage, $P_{bat,req}$: battery required output power, SOC_{min} : minimum SOC, SOC(end): SOC at the end of the mission, N_{series}: number of cells in series, and $N_{parallel}$: number of cells in parallel)

Figure 3 presents a flowchart that outlines the methodology for integrating the EPS models. The modelling process is divided into two parts: the modelling loop for the battery (right-hand side) and the modelling loop for the power consumers (left-hand side). The overall modelling process begins with modelling the motor, which takes its required power output ($P_{out,mot}$), voltage, and rotational speed as inputs. The inverter is then modelled using its power output ($P_{out,inv}$) and current output ($I_{out,inv}$)

from the motor model. The bus is modelled based on the system voltage and its required power output ($P_{out,bus}$), and it supplies the power ($P_{out,con}$) and voltage ($V_{out,con}$) requirements to the battery modelling loop.

In the battery modelling loop, the numbers of cells in series (N_{series}) and in parallel ($N_{parallel}$) are initially assumed, and the initial battery voltage is calculated. The battery is then modelled, and its voltage (V_{bat}) is transmitted to the converter. The modelling of the converter determines the required power output ($P_{bat,req}$) of the battery. For the battery modelling to be successful, the battery voltage needs to be higher than the voltage required ($V_{out,con}$) by the loop, and the battery's state of charge (SOC) at the end of the flight mission should be above the minimum SOC.

The following sections present the modelling methods of the components, and their sequence follows the steps of model integration, which are mentioned above and associated with Figure 3.

2.1 Motor modelling

The major sources of loss for all types of electric motors are the same and can be categorized into four types [27]: 1) copper (ohmic) losses, 2) iron (core) losses, 3) windage and friction losses, and 4) other losses. These losses are dependent on the motor design, rotational speed, and torque.

McDonald [28] presented a loss-based modelling method for the conceptual design of electric motors, referred to as the 'rubber' motor modelling method. This design used the McDonald's motor modelling method, and its motor design parameters were assumed based on [28,29], as listed in Table 2. The motor's loss fractions and losses are calculated as follows:

Table 2 Design parameters of the motor

Parameter	Value
Optimum torque (Nm) Trq'	636.62
Optimum efficiency η'	0.97
Optimum rotational speed (rad/s) ω'	942.48
Parasite loss ratio k_0	0.95
Motor voltage (V)	400

Other losses, which occur regardless of motor torque or rotational speed and even at motor stationary conditions, are given by Eq.(1).

$$C_0 = k_0 * \frac{Trq' * \omega'}{6} * \frac{1-\eta'}{\eta'} \quad (1)$$

Copper (ohmic) losses, which are due to the electrical resistance of the wires inside the motor and are proportional to the motor torque square, are given by Eq.(2).

$$Copper\ losses = k_c * Trq^2 \quad (2)$$

where,

$$k_c = \frac{\omega'(1-\eta')}{2 * Trq' * \eta'} \quad (3)$$

Iron (core) losses, which are due to magnetic effects and are proportional to the motor rotational speed, are given by Eq.(4).

$$Iron\ losses = k_i * \omega \quad (4)$$

where,

$$k_i = \frac{-3C_0}{2\omega'} + \frac{Trq'(1-\eta')}{4\eta'} \quad (5)$$

Windage and friction losses, which are due to the friction torque in the bearings, are given by Eq.(6).

$$Windage\ losses = k_w * \omega^3 \quad (6)$$

where,

$$k_w = \frac{C_0}{2\omega'^3} + \frac{Trq'(1-\eta')}{4\eta' * \omega'^2} \quad (7)$$

Finally, the total loss of the motor is given by Eq.(8), which is the sum of these four losses.

$$Total\ loss = C_0 + k_c * Trq^2 + k_i * \omega + k_w * \omega^3 \quad (8)$$

2.2 Inverter modelling

An inverter, which consists of diodes and power switches (PSs), converts DC to AC. The diodes and PSs are connected in series or parallel within a module, and their numbers are usually the same. Each phase contains two modules, and the number of phases depends on the design of the electrical machine (motor or generator). An inverter can be modelled by the loss-based method presented in [30]. The component parameters of the inverter were assumed based on [30], as shown in Table 3.

In the inverter, both diodes and PSs incur conduction and switching losses. The equations for the loss calculations are referred to [30]. For the three-phase motor, the total loss of the inverter ($P_{loss,total}$) is calculated by Eq.(9).

$$P_{loss,total} = \sum P_{loss} * N_{parallel} * N_{series} * 6 \quad (9)$$

where, N_{series}=the numbers of components connected in series $N_{parallel}$= the numbers of components connected in parallel.

Table 3 Component parameters of the inverter

Parameter	PS	Diode
Switching energy (mJ) E_{ps},E_d	53	195
Threshold voltage (V) V_{ps}, V_d	0.85	1.1
Reference current (I) $I_{ref,ps}$,$I_{ref,d}$	900	900
Reference voltage (V) $V_{ref,ps}$, $V_{ref,d}$	1200	550
Resistance (mΩ) R_{ps},R_d	5.86	4.76
Power factor for voltage $K_{I,ps}$,$K_{I,d}$	-	0.6

Power factor for current $K_{V,ps}$,$K_{V,d}$	1.4	0.6
Threshold voltage (V) V_{ps}, V_d	0.85	1.1
Reference current (I) $I_{ref,ps}$,$I_{ref,d}$	900	900
Reference voltage (V) $V_{ref,ps}$, $V_{ref,d}$	600	600
Resistance (mΩ) R_{ps},R_d	5.86	4.76
Power factor for voltage $K_{I,ps}$,$K_{I,d}$	1.4	1
Power factor for current $K_{V,ps}$,$K_{V,d}$	1.6	1.4

where, the subscript *ps* is power swich, and the subscript *d* is diode.

2.3 Electric bus modelling

The electric bus was modelled using the loss-based method based on Ohm's Law, with the temperature effect on it being neglected. The length of the bus was assumed to be 8.1 m, which corresponds to the wingspan of the ATR72. Aluminium was selected as the material for the bus, and the parameters of the aluminium bus were assumed based on Ref.[31,32], as shown in Table 4. The resistance (R) and heat loss of the bus are calculated using Eq.(10) and Eq.(11), respectively.

Table 4 Component parameters of the bus

Length (m)	8.1
Resistivity (Ω*m)	1.68E-08
Current density (A/mm^2)	0.45

$$R = \frac{resistivity * length}{Ac} = \frac{resistivity * length}{\frac{I_{design}}{J}} \quad (10)$$

$$P_{bus,loss} = I^2 R \quad (11)$$

where, Ac =bus cross-section area, I_{design} =bus design current, J=current density, and I=current.

2.4 DC converter modelling

There are three common types of DC converters [33]:

1. Buck converter: decreases voltage from input to output.
2. Boost converter: increases voltage from input to output.
3. Buck-boost converter: either increases or decreases voltage from input to output.

The buck converter was chosen for this design, considering it has less loss and weight than other types of converters. The component parameters of the buck converter were assumed based on Ref.[30],[33], as shown in Table 5.

The architecture of the DC converter is similar to that of the inverter and rectifier, consisting of power switches (PSs) and diodes. Unlike the inverter, the losses of the converter depend on the input and output voltages, and the equations for the loss calculations are referred to [34]. Finally, the total loss of the DC converter ($P_{loss,total}$) is calculated by Eq.(12).

$$P_{loss,total} = \sum P_{loss} * N_{parallel} * N_{series} \quad (12)$$

where, N_{series}=the numbers of components connected in series $N_{parallel}$= the numbers of components connected in parallel.

Table 5 Component parameters of the converter

Parameter	PS	Diode
Switching energy (mJ) E_{ps},E_d	53	195

where, the subscript *ps* is power swich, and the subscript *d* is diode.

2.5 Battery modelling

A battery pack is composed of battery cells that are connected either in series or in parallel. As shown in Figure 4, the cell voltage of a Lithium-ion (Li-ion) battery decreases when it discharges at constant current and temperature conditions. The battery voltage experiences a sharp drop in what is referred to as the 'exponential zone'. The voltage then remains constant at nominal zone. Finally, the voltage decreases rapidly to zero.

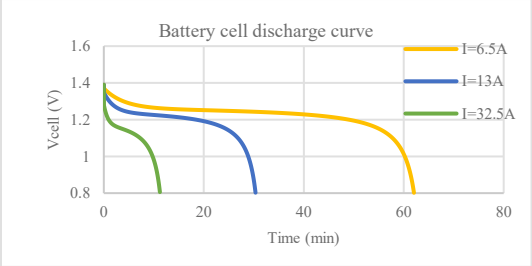


Figure 4 Battery discharge curves at constant currents [35]

The state of charge (SOC) of the battery is defined by Eq.(13). For a Li-ion battery, if the SOC falls below the minimum SOC, it can damage the battery.

$$SOC = \frac{C_{act}}{C_{bat}} \quad (13)$$

where, C_{act} =actual battery capacity, and C_{bat} =total battery capacity.

Figure 5 presents a flowchart of the battery pack modelling process, which involves simulating the battery model across the mission. The modelling process begins by initializing the numbers of cells in series (N_{series}) and in parallel ($N_{parallel}$). The battery full voltage and its total capacity are calculated by Eq.(14) and Eq.(15).

$$V_{bat,full} = V_{cell,full} * N_{series} \quad (14)$$

$$C_{bat,full} = C_{cell,full} * N_{parallel} \quad (15)$$

where, $V_{cell,full}$ =cell full voltage, and $C_{cell,full}$ =cell full capacity.

With the output power profile of the battery pack, the battery cell starts to be modelled in the iterative cell modelling loop. In

this design, the cell was modelled using the improved E-equivalent method described in Ref.[35]. Its component parameters were assumed based on [35], as shown in Table 6. The internal resistance was assumed as constant, neglecting the temperature effect on it.

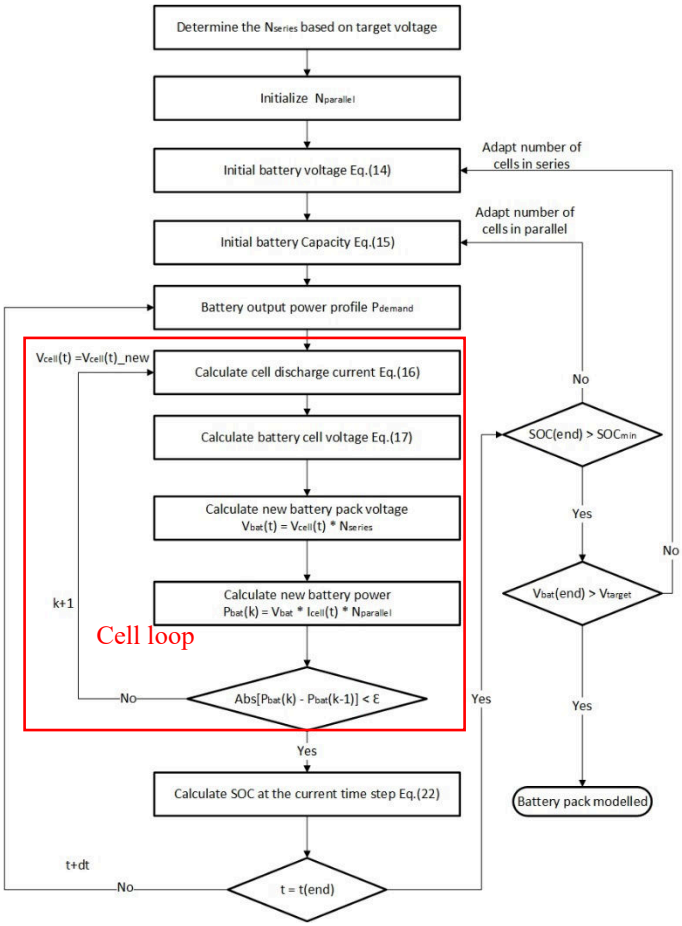


Figure 5 Flowchart of battery pack modelling

Table 6 Component parameters of the battery cell

Parameter	Value
Full capacity (Ah)	2.6
Full voltage (V)	4.2
Exponential zone charge (Ah)	0.1277
Exponential zone voltage (V)	3.889
Nominal current (A)	1.13
Nominal zone charge (Ah)	2.351
Nominal zone charge (V)	3.6
Internal resistance (Ω)	0.01385

The cell discharge current ($I_{cell}(t)$) and new cell voltage ($V_{cell,new}(t)$) at the current time step are calculated by Eq.(16) and Eq.(17). In the first iteration of the cell loop, the $V_{cell}(t)$ is assumed as $V_{cell}(t-1)$.

$$I_{cell}(t) = \frac{P_{demand}}{V_{cell}(t) * N_{series} * N_{parallel}} \quad (16)$$

$$V_{cell,new}(t) = V_0 - I_{cell}(t) * R_{cell} - K\frac{C_{cell,full}}{C_{cell,full} - C_{act}(t)} * (C_{act}(t) + I_{cell}(t)) + Aexp(-B * C_{act}(t)) \quad (17)$$

where,

$$V_0 = V_{cell,full} + R_{cell} * I_{cell}(t) - A \quad (18)$$

$$A = V_{cell,full} - V_{cell,exp} \quad (19)$$

$$B = 3/C_{cell,exp} \quad (20)$$

$$K = \frac{(V_{cell,full} - V_{cell,exp} + A(exp(-B * C_{cell,exp}) - 1))(C_{cell,full} - C_{cell,exp})}{C_{cell,full}(C_{cell,exp} + I_{cell,nom})} \quad (21)$$

where, $V_{cell,exp}$ =cell exponential voltage, $C_{cell,exp}$ =cell exponential capacity, R_{cell}=cell resistance, and $I_{cell,nom}$=cell nominal current.

The battery voltage ($V_{bat}(t)$) and the new battery power ($P_{bat}(k)$) are then calculated. The cell is modelled until the battery power is converged, where the $P_{bat}(k-1)$ equals to the battery power demand (P_{demand}) in the first iteration of the cell loop.

After the cell loop, the battery cell SOC at the current time step is obtained by Eq.(22). At the end of the simulation, if the SOC is above the minimum SOC and the battery pack voltage reaches the target voltage, the process returns the SOC and the battery pack voltage at the end of the power profile, and the battery pack is modelled. If not, the $N_{parallel}$ or N_{series} is adapted and the simulation is restarted.

$$SOC(t) = SOC(t-1) - \frac{I_{cell}(t) * dt}{C_{cell,full}} \quad (22)$$

where, dt=time step.

2.6 TMS design

Figure 6 presents a flowchart of the passive cooling of the TMS design. Once the EPS's model integration is completed, the heat loads of EPS can be obtained, and the TMS design is then initiated. With the ambient temperature and components' temperature limits, the performance of passive cooling is first assessed to investigate if it is sufficient for the component cooling. In this study, the passive cooling mechanism involves air natural convection and radiation, as shown in Figure 7. The performance of the passive cooling is determined based on the heat transfer area of the component. If the passive cooling is not sufficient for the cooling, an active cooling design is then required. This paper only assesses the performance of passive cooling and does not involve the active cooling design.

Considering the effects of installations, temperature limits and heat loads of the EPS components, the TMS was designed by grouping the heat loads into three cooling loops: 1) the motor-inverter (MI) loop, 2) the bus loop, and 3) the battery-converter (BC) loop. As Figure 7 shows, the air natural convection requires enough space for the air flows, and the radiation occurs when the

hot object is not close to another heat source. Therefore, in this study, the passive cooling was not considered for the MI loop due to the proximity of the motor and inverter to other heat sources, such as the engine and the generator, which limits the space available for natural air flows or radiation.

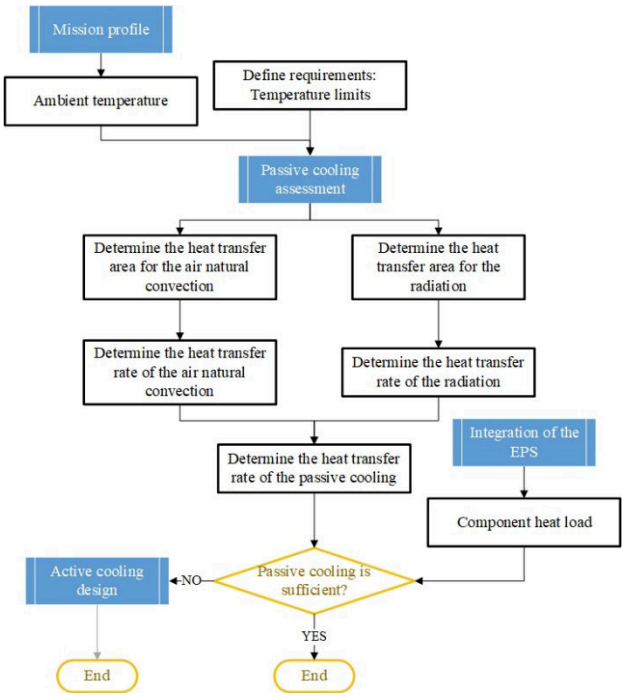


Figure 6 Flowchart of the passive cooling of TMS design

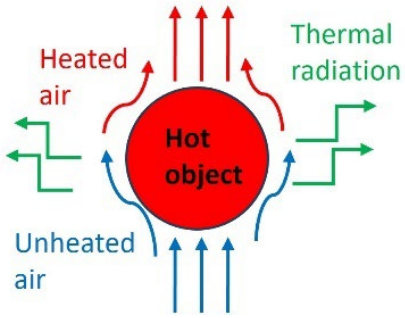


Figure 7 Passive cooling for a hot object

To simplify the assessment of the passive cooling, the geometry of the bus was assumed as a cylinder, and the geometries of the converter and the battery were assumed as boxes. The cross-section area of the bus is obtained by Eq.(10), and its diameter is then determined. The dimensions of the converter and the battery are calculated by a scaling factor, given by Eq.(23) and Eq.(24), respectively. Table 7 presents the geometries and dimensions of the components.

$$Scaling\ factor = \sqrt[3]{\frac{P_{design}}{P_{ref}}} \tag{23}$$

$$Scaling\ factor = \sqrt[3]{\frac{C_{bat}}{C_{ref}}} \tag{24}$$

where, P_{ref}=power output of the reference component, P_{design}=design power of the component, C_{bat}=battery capacity, and C_{ref}=battery capacity of the reference battery.

Table 7 Dimensions and geometries of the electrical components

	Bus	Converter	Battery
Geometry	Cylinder	Box	Box
Ref. component	-	[36]	[37]
Length (cm)	-	84.02	195.53
Width (cm)	-	52.97	156.43
Height (cm)	-	21.92	117.32
Diameter (mm)	6.2	-	-

For the natural air convection, the heat transfer coefficient is dependent on the type of surface, such as vertical or horizontal surfaces. For different surfaces, the heat transfer coefficients (h) are calculated by Eq.(25) and (26), based on Ref.[38]. Their heat transfer rates of natural air convection (Q_{nat}) are then obtained by Eq.(28).

For horizontal surface and cylinder

$$h = 1.32 * \left(\frac{T_s - T_{fluid}}{D_h}\right)^{0.25} \tag{25}$$

For vertical surface,

$$h = 1.42 * \left(\frac{T_s - T_{fluid}}{D_h}\right)^{0.25} \tag{26}$$

For vertical and horizontal surfaces,

$$D_h = \frac{4 * A_{th}}{2 * (length + width)} \tag{27}$$

where, T_s=component surface area, T_{fluid}=fluid temperature, D_h=equivalent hydraulic diameter, and A_{th}=heat transfer area.

$$Q_{nat} = h * A_{th} * (T_s - T_{fluid}) \tag{28}$$

Additionally, the heat transfer rate of radiation ($\mathrm{Q_{rad}}$) is calculated by Eq.(29), based on Ref.[38].

$$Q_{rad} = 0.85 * A_{th} * 5.67 * 10^{-8} * (T_s^4 - T_{fluid}^4) \tag{29}$$

The heat transfer rate of passive cooling (Q_{pass}) is then obtained by Eq.(30).

$$Q_{pass} = Q_{nat} + Q_{rad} \tag{30}$$

Furthermore, the operating temperature limits of the components were assumed based on Ref.[29,31,39], as shown in Table 8.

Table 8 Temperature limits

Component	Tmin (oC)	Tmax (oC)
Motor	-20	220
Inverter	-20	150
Bus	-20	70
Converter	-20	150
Battery	15	45

Figure 8 shows the flowchart of the passive cooling of the TMS design. In the active cooling design, air cooling is given priority because it requires fewer components, resulting in a lighter weight. During the air cooling design, the cold plates for the components are designed based on the assumed sizes. The drag caused by the cold plates is then assessed. If the drag is acceptable the air duct is then designed, and the drag, cooling power, and weight of the TMS are assessed. If the drag is not acceptable, a liquid cooling or phase-change cooling is required. The coolant for the cooling loop is defined, and the cold plates for the components are then designed based on new size assumptions. The heat exchanger of the cooling loop is designed, and the TMS weight, drag, and required power are then assessed, and the required power is supplied to the EPS and the GT system for fuel consumption evaluation. Finally, the optimal coolant and the cooling strategy are obtained by comparing the results of the previous assessments.

3 PROPOSED STUDY

The SMR aircraft under study is similar to ATR 72, which is powered by two PW127 turboshaft engines. According to ATR Company [40] and Jane's [41], the aircraft parameters and propulsion requirements are defined and provided in Table 9.

Table 9 BL aircraft parameters and propulsion requirements

T/O power per engine (kW)	2051
Cruise power per engine (kW)	1589
T/O altitude (m)	0
Cruise altitude (m)	5181.6
T/O time (min)	2
Climb time (min)	17.5

In this study, the baseline (BL) aircraft was hybridised, assuming that the maximum take-off weight (MTOW) and the aerodynamics remain the same. Table 10 shows the specifications for the EPS. The specific weights and the specific energy are assumed based on a 10-year technological level, derived from the values in [29,42]. The peak power of the HEA engine is adjusted from the T/O power to the cruise power of the BL engine. As a result, the EPS provides the supplementary propulsive power for the HEA from T/O to the end of the climb. A typical mission profile (T/O and climb) is proposed in this study to assess the IPTMS platform, as shown in Figure 9.

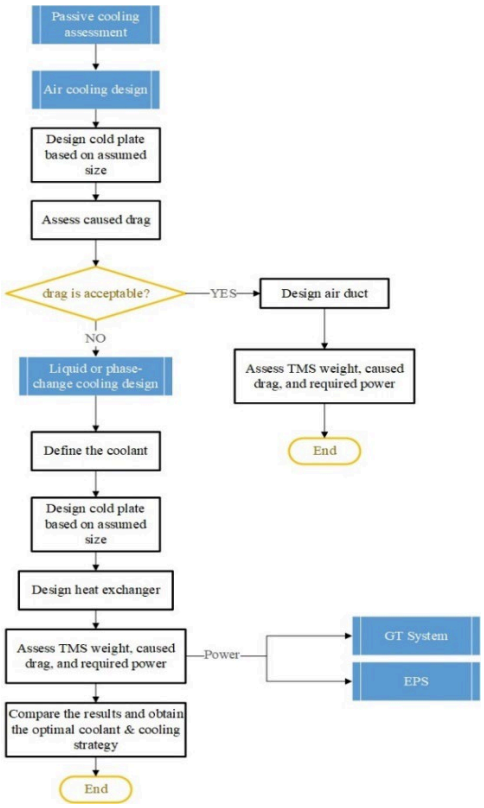


Figure 8 Flowchart of the active cooling of TMS design

Table 10 Specifications for the electrical propulsion system (EPS)

	Design Power (kW)	Design Capacity (kWh)	Specific Weight (kW/kg)	Specific Energy (Wh/kg)
Motor	500	-	15	-
Inverter	600	-	20	-
Bus	930	-	100	-
Converter	950	-	20	-
Battery	-	263	-	400

As shown in Figure 9 (a), (b), and (c), the supplementary power provided by the EPS is assumed to decline linearly from 924 kW to zero during the climb, while the flight altitude and the Mach number increase linearly during the climb phase. Figure 9 (d), (e), and (f) show the variation of ambient temperature under the normal, hot-day, and cold-day conditions. As Figure 9 (c) and (d) show, at the late-climb, the ambient temperature is down to -10 ℃, while the EPS total output power decreases to 200 kW, implying that after this flight segment, the electrical components are likely to be cooled sufficiently by the passive cooling mechanism under the normal condition. Similarly, the ambient temperatures can be down to -3℃ and -30℃ under hot-day and cold-day conditions, respectively, implying that the passive cooling mechanism could also potentially be sufficient under hot-day and cold-day conditions.

The design point (DP) for the IPTMS platform, which is identified as the start of climb (or end of take-off), is the condition where the maximum total heat and power loads of the EPS are expected to occur. At this point, the EPS and TMS components are modelled, and the performance of the EPS and the capabilities of passive cooling are assessed at the mission level for the three scenarios (normal, hot-day, and cold-day conditions).

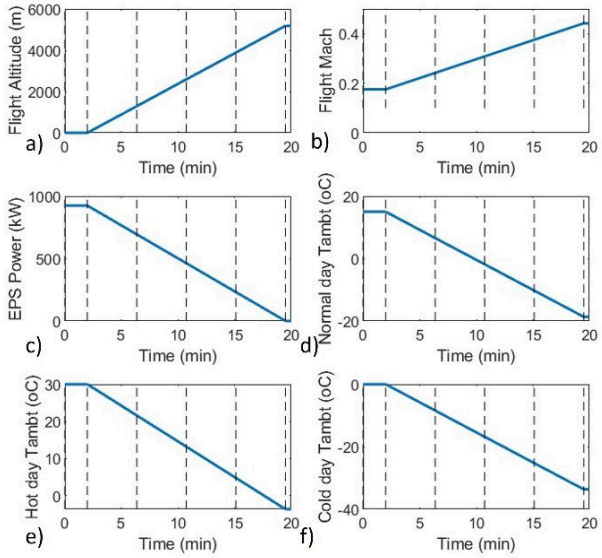


Figure 9 Typical mission profile: a) flight altitude profile, b) flight Mach number profile, c) EPS total output power profile, d) normal-day ambient temperature (Tambt) profile, e) hot-day ambient temperature profile, f) cold-day ambient temperature profile, where the dash lines represent the flight segments in the sequence as follows: takeoff, start-climb, early-climb, mid-climb, late-climb, and end-climb

4 RESULTS ANALYSIS

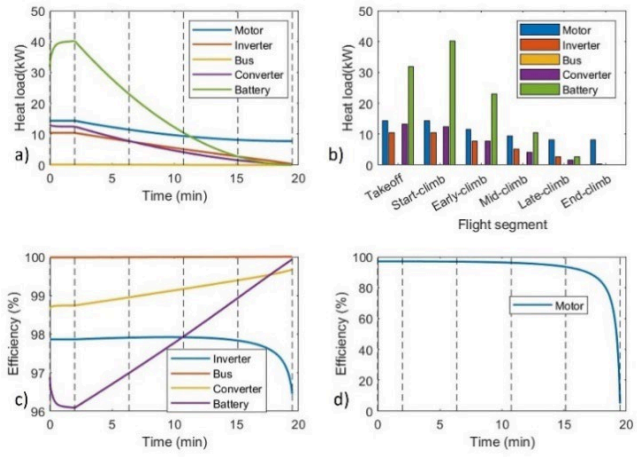


Figure 10 a) EPS heat loads across the mission, b) EPS heat loads per flight segment, c) EPS components' efficiencies excluding motor, d) motor efficiency

Figure 10 shows the assessment for heat loads and efficiencies across the flight mission, while Figure 11 shows the power output of the components per flight segment. As expected, the maximum heat loads of the components occur at the DP condition, as shown in Table 11 and Figure 10 (a). From take-off (T/O) to mid-climb, in the EPS, the battery generates the majority of the heat, reaching up to 40.15 kW at the start-climb (or the DP) condition, as shown in Figure 10 (b). As shown in Figure 10 (c), the efficiencies of the battery, the converter, and the bus increase towards 100%. This is because when the EPS's power required decreases, the system current also decreases, thereby reducing the heat loads. However, the rotational speed of the motor remains constant due to the constant propeller rotational speed of the HEA. In this case, the iron and the windage losses of the motor remain constant, although the required propulsive power declines. As a result, the inverter still needs to provide power to ensure the constant motor speed, causing low efficiency at low-power conditions, shown in Figure 10 (d). At the end-climb, due to the constant rotational speed, the motor still generates 115 kW of power output (shown in Figure 11) and the MI loop generates 8 kW of heat load (shown in Figure 10 (b)), thereby increasing the requirements of future active cooling design at low-power conditions.

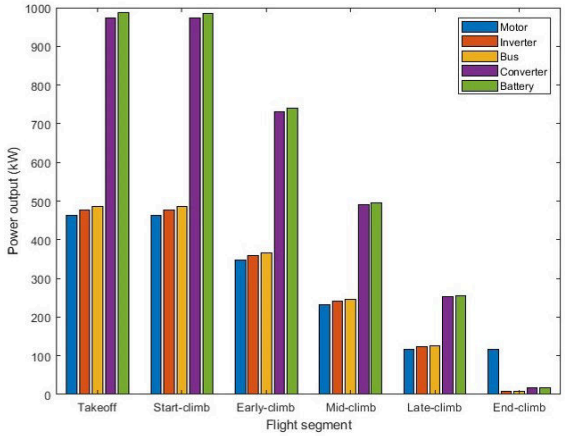


Figure 11 Power output of the components per flight segment

Table 11 Components' heat loads at the design point

Component	Heat load (kW)
Motor	14.33
Inverter	10.42
Bus	0.17
Converter	12.45
Battery	40.15

Table 12 shows the weight comparison between the baseline aircraft and the HEA. Their maximum take-off weights (MTOW) are the same. In this study, the GT engine was not downsized, and its weight remains the same. Therefore, the HEA's propulsion system is 840.97 kg heavier than the baseline aircraft due to the EPS, reducing the other weight. The other weight includes payload weight, fuel weight, TMS weight, etc. In this case, minimizing the TMS weight for the HEA can maximize the carried weight of the aircraft. The passive cooling mechanism can reduce the requirements of TMS, thereby minimizing the TMS weight. Additionally, through the analysis

of the passive cooling, the impact of the electric components' volumes can be evaluated. In this study, although the carried weight of the aircraft is reduced, the fuel weight can be reduced due to the hybridisation which might compensate the negative impact of the increased weight for the HEA.

Table 12 Weight comparison between the baseline aircraft and the HEA

	Baseline Aircraft	HEA
GT Engine Weight (kg)	960	960
EPS Weight (kg)	-	840.97
Other Weight (kg)	21840	20999.03
MTOW (kg)	22800	22800

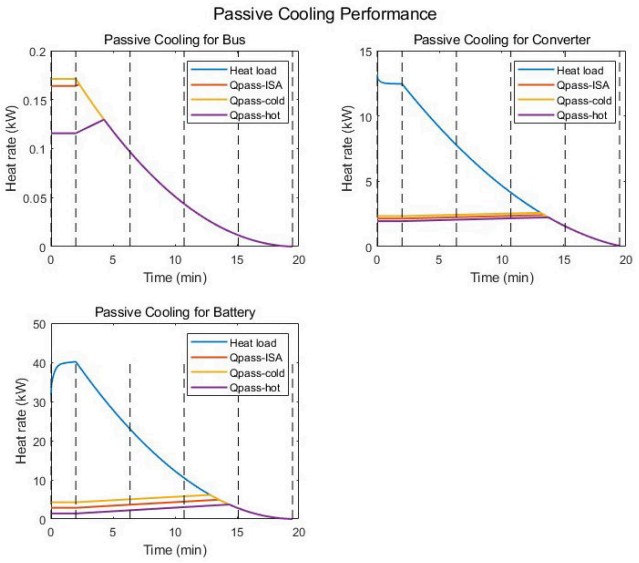


Figure 12 Comparison between the heat load and the passive cooling performance (Qpass) for a) bus, b) converter, and c) battery under the ISA (normal), cold-day, and hot-day conditions

Assuming the components operate at their maximum operating temperature, they can be sufficiently cooled by the passive cooling mechanism under the ISA (normal day), cold-day, and hot-day conditions, as shown in Figure 12. Similarly, Figure 13 shows the variations of the components' surface temperatures under those three operating conditions.

Under the ISA condition, soon after the start of climb, the electric DC bus can be cooled without the need for active cooling at 2.3 minutes. After the mid-climb, the passive cooling is sufficient for the BC loop at 13.4 minutes. As Figure 13 shows, with the sufficient passive cooling in the normal condition, the surface temperatures of bus and converter decreases to -15℃ at the end of the mission within their operating temperature ranges, even when the ambient temperature is -18.68℃ at that flight altitude. Due to the low ambient temperatures at high altitudes, the battery temperature decreases below its minimum operating temperature (15 ℃) after the late-climb segment, which necessitates active temperature control to prevent damage.

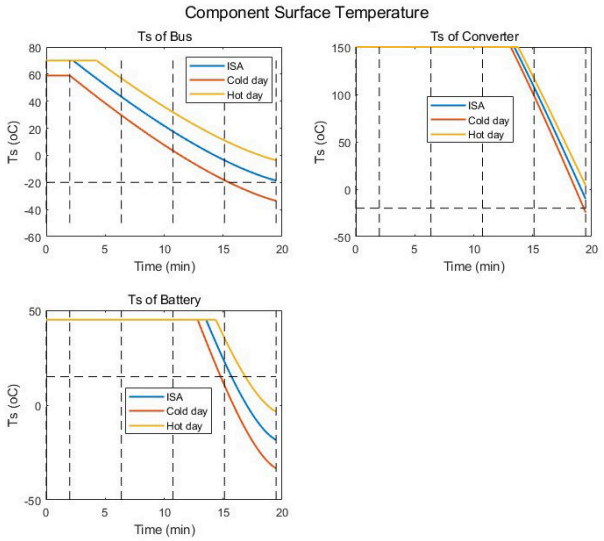


Figure 13 Variations of component surface temperature s(Ts) for: a) bus, b) converter, and c) battery under the ISA, cold-day, and hot-day conditions, where the horizontal dash lines represent the component minimum temperatures

As shown in Figure 12 and Figure 13, the trends of passive cooling performance and components' surface temperatures at the cold-day and hot-day conditions are similar to the results under the normal condition. Compared with the normal condition, the points at which passive cooling is sufficient to cool the component move forward in the hot-day condition and backward in the cold-day condition, respectively. Under the hot-day condition, the bus still requires active cooling until 4 minutes into the mission, while the converter and the battery can be sufficiently cooled by the passive cooling mechanism at 13.5 minutes and 14 minutes, respectively. Under the hot-day condition, the battery temperature is still below its minimum temperature after the late-climb. Under the cold-day condition, the bus can be sufficiently cooled without any need for active cooling across the mission. The passive cooling mechanism is sufficient for the BC loop at about 12.8 minutes. Compared with the normal condition, the temperatures of the bus, the converter, and the battery are below their minimum temperatures after the late-climb, requiring active temperature control. Under the hot-day and cold-day conditions, the points at which the passive cooling mechanism becomes sufficient shift by approximately 1 minute for the BC loop, and around 2 minutes for the bus. This implies that the operating conditions have the most significant impact on the passive cooling for the bus compared to other components. In this scenario, although passive cooling is not feasible for the MI loop, the MI loop does not require active cooling control to prevent temperatures from dropping below their minimum levels, implying that the heat from the GT engines has a positive impact under cold-day and high-altitude conditions.

Table 13 presents the durations of sufficient passive cooling without active temperature control and their corresponding percentages of the typical mission duration. It was observed that the duration of passive cooling for the bus is approximately 78-

88% of the typical mission duration. The converter and the battery durations are around 30% and 10%, respectively. These results also suggest that the passive cooling for the bus is more sensitive to the operating conditions compared to the converter and battery.

Table 13 Durations of sufficient passive cooling without active temperature control and corresponding percentages of time

Component	Duration of passive cooling (min)		
	ISA	Cold day	Hot day
Bus	17.20 (88.28%)	15.47 (79.37%)	15.21 (78.05%)
Converter	6.04 (31.02%)	6.21 (31.85%)	5.72 (29.37%)
Battery	2.15 (11.06%)	1.96 (10.07%)	2.48 (12.71%)

5 CONCLUSION AND FUTURE WORK

Studies in the literature indicate that the HEA requires an IPTMS to prevent its benefits from being offset by additional thermal requirements and weight penalty. This paper addresses these issues by proposing a generic methodology for IPTMS's analytical models and assessing the performance of passive cooling.

In this study, a SMR aircraft similar to the ATR72 is studied. The MTOW and the engine weight of the HEA are assumed to be the same as those of the baseline aircraft, respectively. Compared with the baseline aircraft, the HEA has an additional 840.97 kg of propulsion system weight due to the EPS, which would decrease the space available for other functions, such as payload weight, fuel weight, TMS weight, and so on. Therefore, it is necessary to minimize the TMS weight to compensate for the weight penalty due to the hybridisation.

The passive cooling mechanism can reduce the requirements of active cooling, potentially minimizing the TMS weight. Through the analysis of passive cooling performance, it was found that under the normal condition, the bus and BC loops can be sufficiently cooled by the passive cooling mechanism after the start of the climb and the mid-climb, respectively. However, active temperature control is required after the late-climb segment, as the battery temperature drops below its minimum operating temperature, to prevent damage. The sufficient passive cooling mechanism implies that the requirements of the active cooling can be reduced. Therefore, the IPTMS weight and the energy consumption are potentially minimized in further IPTMS design. Additionally, the MI loop, due to the constant rotational speed, still generates 8 kW of heat load at the end-climb, thereby increasing the requirements of future active cooling design at low-power conditions.

Compared with the normal condition, the points at which the passive cooling is sufficient to cool the component move forward in the hot-day condition and backward in the cold-day condition, respectively. Additionally, compared with other components, operating conditions have the most significant impact on the passive cooling for the bus. Under the hot-day condition, the battery temperature is below its minimum temperature after the late-climb, still requiring active temperature control. Under the cold-day condition, the bus, the converter, and the battery require active temperature control after the late-climb. In this case, the heat from the GT engines has a positive impact at the cold-day condition.

The studied aircraft can be assessed with the integrated model under normal, hot-day, and cold-day conditions for heat and power loads, as well as passive TMS performance. This demonstrates the adaptability of the integrated modelling method. These findings could have implications for the design of more efficient and sustainable aviation systems. Future work will focus on the active cooling design, comparing cooling with and without passive cooling, and further optimisation of the IPTMS platform.

REFERENCES

[1] Directorate-General for Research and Innovation, and Directorate-General for Mobility and Transport, 2012, *Europe's Vision for Aviation: Maintaining Global Leadership and Serving Society's Needs*, European Commission, Luxembourg.

[2] NASA, 2017, *Strategic Implementation Plan 2017 Update*, NASA, Washington, DC.

[3] Rheaume, J. M., and Lents, C. E., 2020, "Commercial Hybrid Electric Aircraft Thermal Management Sensitivity Studies," *AIAA Propulsion and Energy 2020 Forum*, American Institute of Aeronautics and Astronautics, Reston, Virginia, pp. 1–6.

[4] Aerospace Technology Institute, 2019, *Accelerating Ambition Foreword Overview of Priorities Air Transport Vision Market Opportunity Vehicles Propulsion and Power Systems Aerostructures Cross-Cutting Enablers Economic Impact Closing Remarks*.

[5] Ganev, E., and Koerner, M., 2013, "Power and Thermal Management for Future Aircraft."

[6] Roberts, R., and Eastbourn, S., 2014, "Vehicle Level Tip-to-Tail Modeling of an Aircraft," International Journal of Thermodynamics, **17**(2), pp. 107–115.

[7] Misley, A. A., D'Arpino, M., Ramesh, P., and Canova, M., 2021, "A Real-Time Energy Management Strategy for Hybrid Electric Aircraft Propulsion Systems," *AIAA Propulsion and Energy 2021 Forum*, American Institute of Aeronautics and Astronautics, Reston, Virginia.

[8] Chapman, J. W., Hasseeb, H., and Schnulo, S. L., 2020, "Thermal Management System Design for Electrified Aircraft Propulsion Concepts," *AIAA Propulsion and Energy 2020 Forum*, American Institute of Aeronautics and Astronautics, Reston, Virginia, pp. 1–23.

[9] Figliola, R. S., Tipton, R., and Li, H., 2003, "Exergy Approach to Decision-Based Design of Integrated Aircraft Thermal Systems," J Aircr, **40**(1), pp. 49–55.

[10] A, R., Pang, L., Jiang, X., Qi, B., and Shi, Y., 2021, "Analysis and Comparison of Potential Power and Thermal Management Systems for High-Speed Aircraft with an Optimization Method," Energy and Built Environment, **2**(1), pp. 13–20.

[11] Lents, C. E., Hardin, L. W., Rheaume, J., and Kohlman, L., 2016, "Parallel Hybrid Gas-Electric Geared Turbofan Engine Conceptual Design and Benefits Analysis," *52nd AIAA/SAE/ASEE Joint Propulsion Conference*, American Institute of Aeronautics and Astronautics, Reston, Virginia.

[12] Chapman, J. W., Schnulo, S. L., and Nitzsche, M. P., 2020, "Development of a Thermal Management System for Electrified Aircraft," *AIAA Scitech 2020 Forum*, American Institute of Aeronautics and Astronautics, Reston, Virginia.

[13] Cinar, G., Mavris, D. N., Emeneth, M., Schneegans, A., and Fefermann, Y., 2017, "Development of Parametric Power Generation and Distribution Subsystem Models at the Conceptual Aircraft Design Stage," *55th AIAA Aerospace Sciences Meeting*, American Institute of Aeronautics and Astronautics, Reston, Virginia.

[14] Schnulo, S. L., Chapman, J. W., Hanlon, P., Hasseeb, H., Jansen, R., Sadey, D., Sozer, E., Jensen, J., Maldonado, D., Bhamidapati, K., Heersema, N., Antcliff, K., Frederick, Z. J., and Kirk, J., 2020, "Assessment of the Impact of an Advanced Power System on a Turboelectric Single-Aisle Concept Aircraft," *AIAA Propulsion and Energy 2020 Forum*, American Institute of Aeronautics and Astronautics, Reston, Virginia, pp. 1–18.

[15] Heersema, N., and Jansen, R., 2022, "Thermal Management System Trade Study for SUSAN Electrofan Aircraft," *AIAA SCITECH 2022 Forum*, American Institute of Aeronautics and Astronautics, Reston, Virginia.

[16] Coutinho, M., Afonso, F., Souza, A., Bento, D., Gandolfi, R., Barbosa, F. R., Lau, F., and Suleman, A., 2023, "A Study on Thermal Management Systems for Hybrid–Electric Aircraft," Aerospace, **10**(9), p. 745.

[17] Rheaume, J. M., MacDonald, M., and Lents, C. E., 2019, "Commercial Hybrid Electric Aircraft Thermal Management System Design, Simulation, and Operation Improvements," *AIAA Propulsion and Energy 2019 Forum*, American Institute of Aeronautics and Astronautics, Reston, Virginia.

[18] Annapragada, R., Sur, A., Mahmoudi, R., Macdonald, M., and Lents, C. E., 2018, "Hybrid Electric Aircraft Battery Heat Acquisition System," *2018 AIAA/IEEE Electric Aircraft Technologies Symposium*, American Institute of Aeronautics and Astronautics, Reston, Virginia.

[19] Kim, J. H., Kwon, K. S., Roy, S., Garcia, E., and Mavris, D., 2018, "Megawatt-Class Turboelectric Distributed Propulsion, Power, and Thermal Systems for Aircraft," *AIAA Aerospace Sciences Meeting, 2018*, American Institute of Aeronautics and Astronautics Inc, AIAA.

[20] Abolmoali, P. C., Donovan, A. B., Patnaik, S. S., McCarthy, P., Dierker, D., Jones, N., and Buettner, R., 2020, "Integrated Propulsive and Thermal Management System Design for Optimal Hybrid Electric Aircraft Performance," *AIAA Propulsion and Energy 2020 Forum*, American Institute of Aeronautics and Astronautics, Reston, Virginia, pp. 1–17.

[21] Shi, M., Sanders, M., Alahmad, A., Perullo, C., Cinar, G., and Mavris, D. N., 2020, "Design and Analysis of the Thermal Management System of a Hybrid Turboelectric Regional Jet for the NASA ULI Program," *AIAA Propulsion and Energy 2020 Forum*, American Institute of Aeronautics and Astronautics, Reston, Virginia, pp. 1–24.

[22] Sergent, A., Ramunno, M., D'Arpino, M., Canova, M., and Perullo, C., 2020, "Optimal Sizing and Control of Battery Energy Storage Systems for Hybrid Turboelectric Aircraft."

[23] Perullo, C., Alahmad, A., Wen, J., D'Arpino, M., Canova, M., Mavris, D. N., and Benzakein, M. J., 2019, "Sizing and Performance Analysis of a Turbo-Hybrid-Electric Regional Jet for the NASA ULI Program," *AIAA Propulsion and Energy 2019 Forum*, American Institute of Aeronautics and Astronautics, Reston, Virginia.

[24] Kellermann, H., Lüdemann, M., Pohl, M., and Hornung, M., 2020, "Design and Optimization of Ram Air–Based Thermal Management Systems for Hybrid-Electric Aircraft," Aerospace, **8**(1), p. 3.

[25] Adler, E. J., Brelje, B. J., and Martins, J. R. R. A., 2022, "Thermal Management System Optimization for a Parallel Hybrid Aircraft Considering Mission Fuel Burn," Aerospace, **9**(5), p. 243.

[26] Schiltgen, B. T., and Freeman, J., 2019, "ECO-150-300 Design and Performance: A Tube-and-Wing Distributed Electric Propulsion Airliner," *AIAA Scitech 2019 Forum*, American Institute of Aeronautics and Astronautics, Reston, Virginia.

[27] Larminie, J., and Lowry, J., 2012, "Electric Machines and Their Controllers," *Electric Vehicle Technology Explained*, Wiley, pp. 145–185.

[28] McDonald, R. A., 2014, "Electric Propulsion Modeling for Conceptual Aircraft Design," *52nd Aerospace Sciences Meeting*, American Institute of Aeronautics and Astronautics, Reston, Virginia.

[29] Haran, K., Krein, P., Pilawa, R., Colravy, K., Lee, D., Zhang, X., Yoon, A., and Yi, X., 2017, *High Speed, High Frequency Air-Core Machine and Drive*, NASA Grant Number: NNX14AL79A, Annual Review.

[30] Vratny, P. C., Forsbach, P., Seitz, A., and Hornung, M., 2014, "Investigation of Universally Electric Propulsion Systems for Transport Aircraft," *29th Congress of the International Council of the Aeronautical Sciences*, pp. 1–13.

[31] Roselco, 2023, "Copper and Aluminium Bus Bars for Currents up to 300000A," Russian Electrotechnical Company [Online]. Available: http://www.roselco.ru/english/products/busbars_%26_power_connections/copper-and-aluminium-bus-bars-for-currents-up-to-300000a/. [Accessed: 05-Sep-2023].

[32] Wilson Power Solutions, 2018, *White Paper: Aluminium Vs Copper*, WPS, Leeds.

[33] S. Roberts, 2016, *DC/DC Book of Knowledge*, RECOM Engineering GmbH & Co KG, Gmunden, Austria.

[34] Wintrich, A., Nicolai, U., Tursky, W., and Reimann, T., 2015, *Application Manual Power Semiconductors*, ISLE Verlag, Nuremberg, Germany.

[35] Tremblay, O., and Dessaint, L.-A., 2009, "Experimental Validation of a Battery Dynamic Model for EV Applications," World Electric Vehicle Journal, **3**(2), pp. 289–298.

[36] Qasim, M. M. , Otten, D. M., Spakovszky, Z. S., Lang, J. H., and Kirtley, J. L., 2023, "Design and Optimization of an Inverter for a One-Megawatt Ultra-Light Motor Drive," AIAA Aviation Forum 2023.

[37] VOLTAI, 2023, "500KW 300kw 1MW Stationary Battery Storage Commercial Battery Energy Storage System Container," Voltai Green Energy Co.,Ltd [Online]. Available: https://www.voltaienergy.com/bess_container/show-98.html. [Accessed: 28-Nov-2023].

[38] Cengel, Y. A., 1997, *Introduction to Thermodynamics and Heat Transfer*, McGraw-Hill, Boston, MA.

[39] Gkoutzamanis, V. G., Tsentis, S. E., Valsamis Mylonas, O. S., Kalfas, A. I., Kyprianidis, K. G., Tsirikoglou, P., and Sielemann, M., 2022, "Thermal Management System Considerations for a Hybrid-Electric Commuter Aircraft," J Thermophys Heat Trans, **36**(3), pp. 650–666.

[40] ATR Aircraft, 2022, "ATR 72-600" [Online]. Available: https://www.atr-aircraft.com/our-aircraft/atr-72-600/. [Accessed: 18-Oct-2022].

[41] Jane's, 2022, "P&WC PW100," Jane's [Online]. Available: https://customer.janes.com/Janes/Display/JAE_0484-JAE_. [Accessed: 07-Nov-2022].

[42] Bertrand, P., Spierling, T., and Lents, C. E., 2019, "Parallel Hybrid Propulsion System for a Regional Turboprop: Conceptual Design and Benefits Analysis," *AIAA Propulsion and Energy 2019 Forum*, American Institute of Aeronautics and Astronautics, Reston, Virginia.

DSPACE

https://dspace.org/

Integrated power and thermal management system for a hybrid-electric aircraft: integrated modelling and passive cooling analysis

Ouyang, Zeyu; Nikolaidis, Theoklis; Jafari, Soheil

2024-11-01
American Society of Mechanical Engineers (ASME)
https://doi.org/10.1115/1.4066050
Ouyang Z, Nikolaidis T, Jafari S. (2024) Integrated power and thermal management system for a hybrid-electric aircraft: integrated modelling and passive cooling analysis. Journal of Engineering for Gas Turbines and Power, Volume 146, Issue 11, November 2024, Paper number GTP-24-1290

Downloaded from a DSpace repository. https://dspace.org/